Neutron crystallography of copper amine oxidase reveals keto/enolate interconversion of the quinone cofactor and unusual proton sharing

Takeshi Murakawa[a,1], Kazuo Kurihara[b], Mitsuo Shoji[c,d], Chie Shibazaki[b], Tomoko Sunami[b], Taro Tamada[b], Naomine Yano[e], Taro Yamada[e], Katsuhiro Kusaka[e], Mamoru Suzuki[f], Yasuteru Shigeta[c], Ryota Kuroki[g], Hideyuki Hayashi[h], Takato Yano[a], Katsuyuki Tanizawa[i], Motoyasu Adachi[b], and Toshihide Okajima[h,i,1]

[a]Department of Biochemistry, Osaka Medical College, 569-8686 Takatsuki, Osaka, Japan; [b]Institute for Quantum Life Science, National Institutes for Quantum and Radiological Science and Technology, 319-1106 Tokai, Ibaraki, Japan; [c]Center for Computational Sciences, University of Tsukuba, 305-8577 Tsukuba, Ibaraki, Japan; [d]Japan Science and Technology Agency (JST), Precursory Research for Embryonic Science and Technology (PRESTO), 332-0012 Kawaguchi, Saitama, Japan; [e]Frontier Research Center for Applied Atomic Sciences, Ibaraki University, 319-1106 Tokai, Ibaraki, Japan; [f]Institute for Protein Research, Osaka University, 565-0871 Suita, Osaka, Japan; [g]Quantum Beam Science Center, Japan Atomic Energy Agency, 319-1195 Tokai, Ibaraki, Japan; [h]Department of Chemistry, Osaka Medical College, 569-8686 Takatsuki, Osaka, Japan; and [i]Institute of Scientific and Industrial Research, Osaka University, 567-0047 Ibaraki, Osaka, Japan

Edited by Perry Allen Frey, University of Wisconsin-Madison, Madison, WI, and approved March 31, 2020 (received for review December 23, 2019)

Recent advances in neutron crystallographic studies have provided structural bases for quantum behaviors of protons observed in enzymatic reactions. Thus, we resolved the neutron crystal structure of a bacterial copper (Cu) amine oxidase (CAO), which contains a prosthetic Cu ion and a protein-derived redox cofactor, topa quinone (TPQ). We solved hitherto unknown structures of the active site, including a keto/enolate equilibrium of the cofactor with a nonplanar quinone ring, unusual proton sharing between the cofactor and the catalytic base, and metal-induced deprotonation of a histidine residue that coordinates to the Cu. Our findings show a refined active-site structure that gives detailed information on the protonation state of dissociable groups, such as the quinone cofactor, which are critical for catalytic reactions.

copper amine oxidase | neutron crystallography | proton sharing | quinone cofactor | metal-induced deprotonation

Protons play crucial roles in chemical reactions that occur in solution, including those catalyzed by enzymes (1). In particular, proton transfers with electron movements are key to the reaction mechanisms of redox enzymes, such as copper amine oxidases (CAOs). Although X-ray crystallography has been used to specify positions of nonhydrogen atoms in protein structures, positions of covalently bound hydrogen (H) atoms and noncovalently bound protons are not easily determined, even at atomic resolution. Neutron crystallography is the only diffraction method that can be used to visualize bound H atoms and protons across entire structures and thereby discloses unusual proton networks and protein structures that have not been resolved using other methods (2–4).

We determined the neutron crystal structure of CAO from *Arthrobacter globiformis* (AGAO; Fig. 1*A*). The CAO family enzymes catalyze the oxidative deamination of various primary amines and produce corresponding aldehydes, H peroxide, and ammonia (5). Currently, all structurally characterized CAOs are homodimers of 70–95-kDa subunits, each containing a Cu^{2+} ion and the protein-derived quinone cofactor topa quinone (TPQ) (5). TPQ has a planar ring structure and a visible absorption band around 480 nm, reflecting the presence of a conjugated π-electron system. The catalytic reaction of CAO starts with a reductive half-reaction in which the oxidized form of TPQ accepts $2e^-$ and $2H^+$ from the substrate amine. Subsequently, the oxidative half-reaction proceeds with the transfer of $2e^-$ and $2H^+$ to molecular oxygen (O), resulting in reoxidation of the cofactor. Our experiments with AGAO demonstrated that stereospecific abstraction of the substrate α-proton in the reductive half-reaction is driven by quantum mechanical tunneling rather than by the classical transition-state mechanism (6). Due to the involvement of protons, the reaction is significantly influenced by solution pH, and, therefore, the protonation state of dissociable groups in the catalytic center (7, 8).

In this paper, we present the neutron crystal structure of AGAO and describe the coexistence of two forms of TPQ and the protonation states of active-site dissociable groups, including the cofactor.

Results and Discussion

Structural Evidence of the Keto Form Cofactor. Using a modified hanging method (*SI Appendix*, Fig. S1*A*), high quality and extra large AGAO crystals (Fig. 1*B* and *SI Appendix*, Fig. S1*B*) were prepared and subjected to deuteration and cryoprotection

Significance

Neutron protein crystallography can visualize bound hydrogen (H) atoms and protons across entire structures, which are generally invisible by X-ray crystallography. In all X-ray crystal structures of CAOs determined so far, the cofactor TPQ has been modeled based on the first identified chemical structure, i.e., an enolate form with a planar quinone ring. Yet our high-resolution neutron crystallography of a bacterial CAO has revealed a keto form cofactor, which exists in equilibrium with the enolate form, both having a nonplanar quinone ring. The neutron structure also indicates a triply shared proton, which would provide a structural basis for quantum behaviors of protons often observed in enzymatic reactions, hitherto unexplained.

Author contributions: T.M., K. Kurihara, R.K., K.T., M.A., and T.O. designed research; T.M., K. Kurihara, M. Shoji, C.S., T.S., T.T., N.Y., T. Yamada, K. Kusaka, M. Suzuki, Y.S., R.K., M.A., and T.O. performed research; N.Y., T. Yamada, and K. Kusaka contributed new reagents/analytic tools; T.M., K. Kurihara, M. Shoji, N.Y., T. Yamada, K. Kusaka, H.H., T. Yano, K.T., M.A., and T.O. analyzed data; T.M., K. Kurihara, M. Shoji, H.H., T. Yano, K.T., M.A., and T.O. wrote the paper; T.M., K. Kurihara, C.S., T.S., T.T., N.Y., T. Yamada, K. Kusaka, M. Suzuki, R.K., M.A., and T.O. carried out diffraction experiments; and M. Shoji and Y.S. performed QM/MM calculation.

The authors declare no competing interest.

This article is a PNAS Direct Submission.

Data deposition: Atomic coordinates and structure factors of the AGAO neutron structure have been deposited in the Protein Data Bank (http://www.rcsb.org/) (accession no. 6L9C).

[1]To whom correspondence may be addressed. Email: murakawa@osaka-med.ac.jp or tokajima@sanken.osaka-u.ac.jp.

This article contains supporting information online at https://www.pnas.org/lookup/suppl/doi:10.1073/pnas.1922538117/-/DCSupplemental.

First published May 5, 2020.

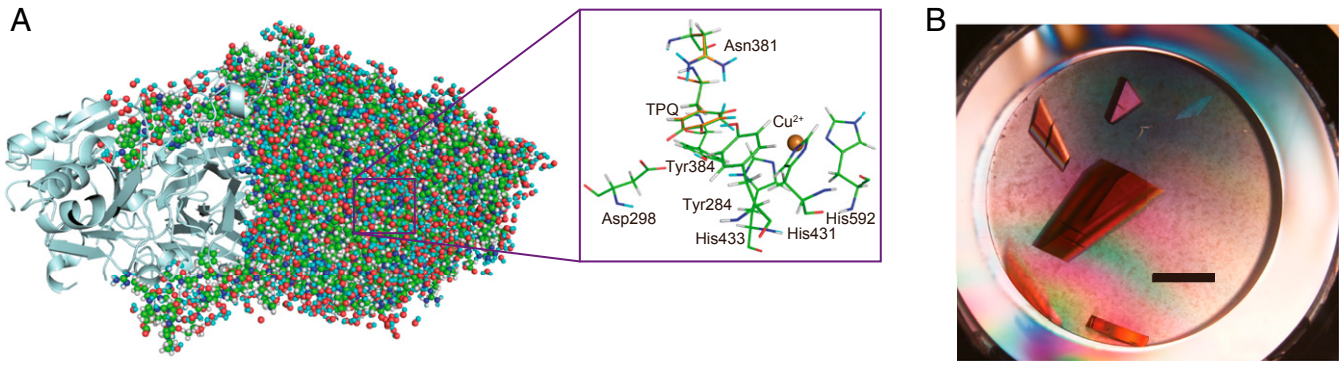

Fig. 1. Neutron/X-ray crystal structure of AGAO. (*A*) The dimer structure of AGAO is shown using a space-filling model for one monomer and a ribbon model for the other; H (white), deuterium (D) (cyan), carbon (green), O (red), nitrogen (N) (blue), and sulfur (yellow) atoms are indicated. Enlarged view; an active-site stick model. (*B*) The huge AGAO crystal used in neutron crystallography; black bar, 2 mm.

through postcrystallization treatments using malonic acid in D_2O. Neutron and X-ray diffraction data at 1.72- and 1.14-Å resolutions, respectively, were collected and used for joint structural refinement. In the crystal structure of AGAO at pD 7.4, we identified almost all nonexchangeable H atoms of the protein and those exchanged by deuterium (D) atoms derived from solvent D_2O (*SI Appendix*, Table S1 and Fig. 1*A*). The AGAO subunit (74 kDa/628 residues) is currently the largest neutron crystallographic structure to be reported, extensively exceeding the molecular mass of previously recorded proteins (*SI Appendix*, Fig. S2). Including noncovalently bound protons, the present AGAO structure comprises 5,198 non-H atoms and 5,823 H/D atoms. This structure unambiguously indicates the protonation state of dissociable groups and the H-bonding (HB) networks of the entire protein.

Striking features were found in and around the active-site cofactor TPQ. We modeled TPQ using both electron density (ED) and neutron scattering length density (SLD) maps (Fig. 2*A*). Unlike previous models, the resulting model of TPQ shows a slightly bent structure with a nonplanar quinone ring (see *SI Appendix*, Fig. S3 *A* and *C* for TPQ models and estimated dihedral angles, respectively). Moreover, positive SLD showed an ellipsoidal shape that expands beside the C3 position and is perpendicular to the TPQ plane (Fig. 2*B*), which is absent in ED maps (not shown). The positive SLD was significantly large and assignable to multiple D atoms with partial occupancies. Taken together, these maps show that there are two forms of TPQ, one with two D atoms attached to the C3 carbon, forming an sp^3 hybridization structure, and the other with one D atom attached in plane to the C3 carbon. We conclude that the keto form of TPQ is generated by protonation/deuteronation of the enolate form, which has long been the accepted chemical structure of oxidized TPQ (Fig. 2*C*). In contrast, the pink color of the AGAO crystal (Fig. 1*B*) indicates the conventional enolate form of the cofactor because the keto form in which the conjugated system is partially broken is not expected to absorb in the visible spectrum. Indeed, calculations with time-dependent DFT (density functional theory) B3LYP/6–311+G* showed an absorption maximum at 258 nm for the keto form of TPQ. By releasing the restraint for planarity of the quinone ring, we refined the TPQ structure as an equilibrated mixture of keto (41%) and enolate forms (59%). In both forms, the bent ring of TPQ fitted easily into the high-resolution ED map (at 1.14 Å). The covalently bound D atoms of TPQ C3 are, therefore, considered products of deuteronation (equivalent to protonation) to C3 of the enolate form of the cofactor from solvent D_2O, followed by deprotonation and subsequent deuteronation (Fig. 2*C*). It is clear that the deuteronation slowly proceeds in a nonstereospecific manner during dialysis of the crystals against the D_2O buffer, leading to di-deuteration of the C3 methylene group of the keto form. A deuteron is thought to be accessible to C3 from either of the two sides of TPQ. This exchange reaction of covalently bound TPQ C3 H atoms with a solvent is probably dependent on the pH (pD) of the crystallization (and deuteration) buffer, but this dependence remains to be studied. The carbonyl and amino moieties of the side-chain amide group of Asn381, which is located over the TPQ ring and restricts its mobility, also showed similar levels of SLD, even though the amino moiety of the amide group generally shows larger SLD due to di-deuteration of a N atom. We suggest that the side-chain amide group of Asn381 has two conformers (Fig. 2*B* and *SI Appendix*, Fig. S4), which are hardly identified by X-ray crystallography. Thus, we determined refined occupancies of 56% and 44% for conformers *a* and *b*, respectively, which are related through flipping around the Cβ–Cγ axis (*SI Appendix*, Fig. S4). In the enolate form of TPQ, the conformer *a* of Asn381 is likely stabilized by a HB with the main chain carbonyl of Val405 (*SI Appendix*, Fig. S4*A*). However, steric hindrance is induced between the C3 D atoms of the keto form of TPQ and the amide protons of the Asn381 side chain, causing flipping of the amide group (conformer *b*; *SI Appendix*, Fig. S4*B*). Thus, the content of the alternative conformer *b* of Asn381 (44%) is comparable to that of the keto form of TPQ (41%).

Identification of a Triply Shared Proton Between the TPQ and the Catalytic Base. Present studies have shown the presence of residual positive SLD with a spherical shape between the TPQ and a conserved Asp residue (Asp298) that has been proposed to act as a catalytic base (ref. 7 and Fig. 3). We temporarily assigned a water molecule (D_2O) in accordance with this SLD, but a water molecule was excluded due to the complete absence of accompanying ED and insufficient distances from neighboring atoms. Thus, we finally assigned an ionized D atom (deuteron, D^+) with an occupancy of 1.0 for this SLD. Although this D resides in an almost coplanar configuration with the two O atoms (Oδ1 and Oδ2) and the Cγ atom of Asp298, distances from Oδ1 (2.0 Å), Oδ2 (1.6 Å), or O5 of TPQ (1.6 Å) far exceed the typical O–H covalent bond distance (approximately 0.95 Å) but are clearly shorter for Asp298 Oδ2 and TPQ O5 than the H(D)-acceptor O distance of 1.8–2.6 Å for ordinary HBs (ref. 9 and Fig. 3). In addition, because the distance between O5 of TPQ and Oδ1 (3.5 Å) or Oδ2 (2.7 Å) of Asp298 is longer than that of low-barrier HBs ([LBHBs]; 2.2–2.5 Å; ref. 10), the deuteron from solvent D_2O between TPQ and Asp298 cannot be interpreted as a shared proton in LBHBs. Collectively, these data suggest that the D^+ ion (H^+ in H_2O) detected in this study as a triply shared

BIOCHEMISTRY

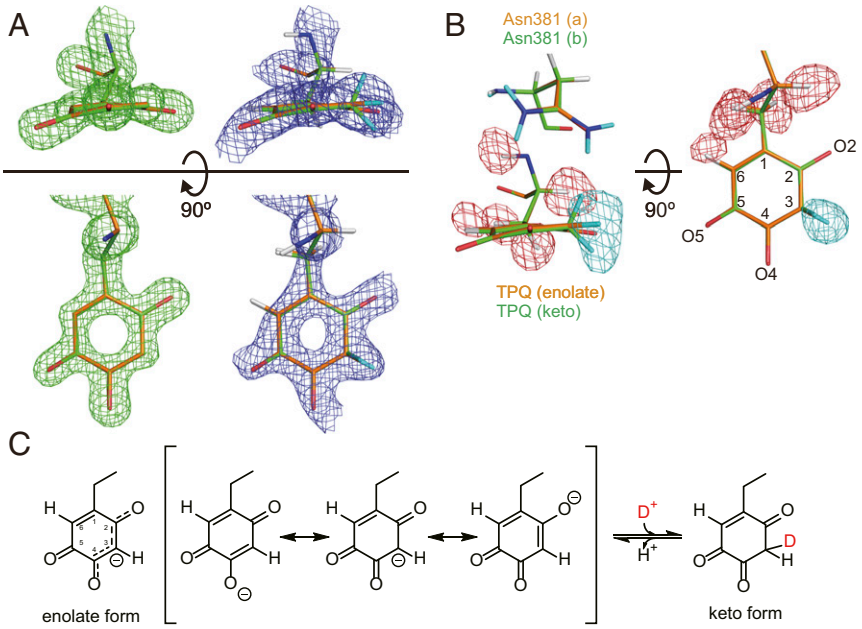

Fig. 2. Neutron/X-ray structure of the cofactor TPQ and its equilibrium state. (*A*) $2F_o - F_c$ ED maps (*Left*, 1.3 σ) and $2F_o - F_c$ SLD maps (*Right*, 1.1 σ) are contoured with stick models for enolate (orange) and keto (green) forms of TPQ. (*B*) $F_o - F_c$ omit SLD maps, calculated without contributions of H and D atoms of TPQ, are contoured with positive (cyan) and negative (red) contours of 3.2 and −2.8 σ, respectively; stick models for enolate (orange) and keto (green) forms of TPQ. In the *Left*, the conformers *a* (orange) and *b* (green) of Asn381(*SI Appendix*, Fig. S4) are shown as stick models. H atoms, white; D atoms, cyan. (*C*) The equilibrium between the enolate and the keto forms of TPQ is shown with the conjugated π-electron system.

deuteron (proton) in an atypically short HB. We also suggest that it is delocalized among the three O atoms of TPQ O5 and the Asp298 carboxyl group (although slightly shifted toward TPQ O5 and Asp298 Oδ2) and connects these moieties in a trifurcated HB that is stronger than canonical HBs but is weaker than those in LBHBs. In contrast, TPQ O2 and O4 atoms are anchored to two water molecules (W1 and an axially Cu^{2+}-coordinating water [W_{ax}]) and to the phenolic OH of Tyr284, respectively, by HBs (Fig. 4*A*). Hence, it is assumed that the strong interaction of the triply shared proton is responsible for the force that bends the quinone ring, albeit slightly, as described below. Similar triply shared protons have been observed in the neutron structure of *Helicobacter pylori* 5′-methylthioadenosine nucleosidase (11).

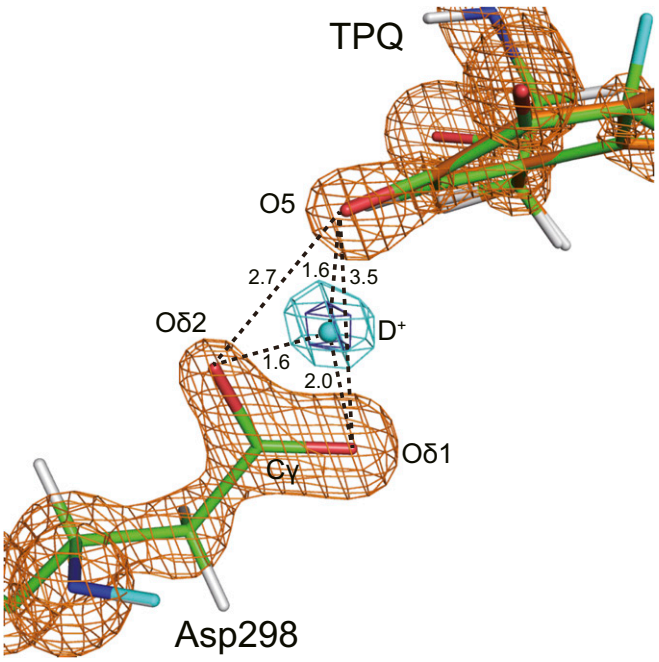

Fig. 3. A triply shared proton between the cofactor and the catalytic base. An $F_o - F_c$ omit ED map, calculated without contributions of TPQ and Asp298, is shown in orange at 8.0 σ. An $F_o - F_c$ omit SLD map, calculated without contributions from the delocalized deuteron, is drawn in dark blue (4.9 σ) and cyan (4.2 σ) with respective distances (Å).

Metal-Induced Histidine Deprotonation. An unusual protonation state was also found around the prosthetic metal ion Cu^{2+}, which is coordinated by three histidine residues (His431, His433, and His592), W_{ax}, and a water molecule that equatorially coordinates to Cu^{2+} (W_{eq}) in a distorted pyramidal geometry as shown in a previous X-ray structure (12). Our SLD map showed that the three imidazole side chains coordinate to Cu^{2+} through lone pairs of deprotonated Nε2 of His431, Nε2 of His433, and Nδ1 of His592 (Fig. 4*B*). The other N atoms of the imidazole are singly deuterated for His433 and His592. However, the SLD of the Hδ1 of His431 was undetectable (Fig. 4*B*). Because SLD and ED were clearly detected for all other atoms of His431, we can rule out disorder of His431 and cancellation of the SLD by partial exchange of D/H (4). We assigned His431 as an imidazolate anion (fully deprotonated form) despite its extremely high pK_a (~14) for the second proton dissociation (ref. 13 and *SI Appendix*, Fig. S5). Cu^{2+} can attract electrons of imidazole rings, leading to significantly lower apparent pK_a (metal-induced histidine deprotonation; ref. 14). Thus, His431 should have a pK_a of the second proton dissociation that is considerably lower than the pH (pD) of the crystallization and deuteration buffers (7.4). For His433 and His592, the pK_a lowering effect of Cu^{2+} may be compensated considerably by HBs with strongly proton-accepting side-chain O atoms of Tyr384 and Asp598, respectively. Yet for His431, only the main-chain carbonyl O atom of Pro429 has weakly proton-accepting properties within a HB distance (Fig. 4*A*). In addition to the Cu site, all other His side

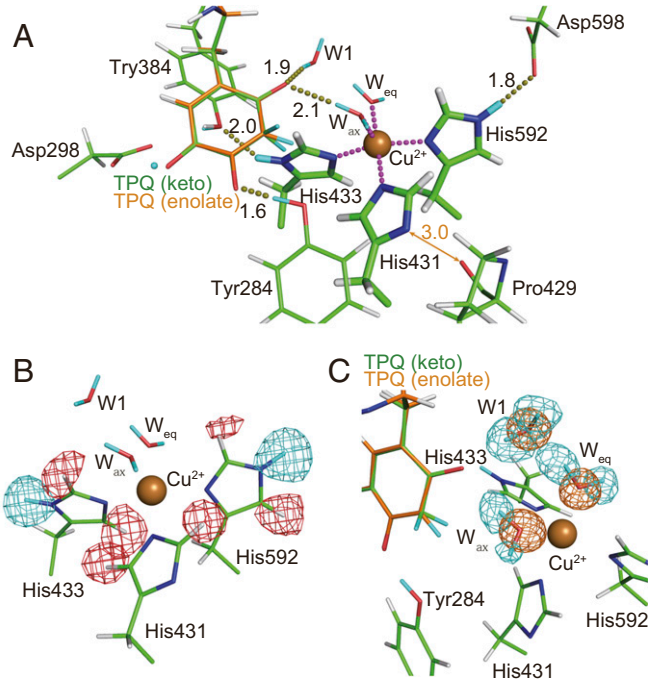

Fig. 4. Active-site structure determined by neutron crystallography. (*A*) Active-site H-bond network and Cu^{2+}-coordination structure. Brown and magenta dotted lines represent H bonds and coordination bonds to Cu^{2+}, respectively, with distances (Å) between the atoms. A solid arrow indicates the distance (Å) mentioned in the text. H atoms, white; D atoms, cyan. (*B*) Cu^{2+}-binding histidine residues and water molecules. $F_o - F_c$ omit SLD maps, calculated without contributions of H and D atoms of the side chain of histidine residues (His431, His433, and His592), are contoured with positive (cyan) and negative (red) contours of 3.5 and −3.0 σ, respectively. (*C*) SLD and ED maps of active-site water molecules. $F_o - F_c$ omit SLD maps, calculated without contributions of D atoms of water molecules (W_{ax}, W_{eq}, and W1), are drawn at 5.0 σ (cyan). $F_o - F_c$ omit ED maps, calculated without contributions from O atoms of W_{ax}, W_{eq}, and W1, are drawn at 7.0 σ (orange).

chains are singly or doubly deuterated in AGAO. These findings from our high-resolution SLD map provide structural evidence for metal-induced deprotonation (15). Similar pK_a-lowering effects were also found for W_{ax} as indicated by significantly lower positive SLD for one of the two D atoms (Fig. 4*C*). Although the pK_a value of bulk water is 14 (16), the water molecule that axially coordinates to the Cu^{2+} ion may have a markedly lowered pK_a value of 7.5 (16), which is close to the data collection pD of 7.4. The partially deprotonated state of W_{ax} (hydroxide ion) is discussed later in the context of possible roles as a proton acceptor.

Quantum Mechanics/Molecular Mechanics Analysis of the Active-Site Structure. To assess the energetic feasibility of the active-site structure including the keto/enolate forms of TPQ, the nonplanar quinone ring, and the triply shared proton, hybrid quantum mechanics/molecular mechanics (QM/MM) calculations were performed using a QM region that covers several active-site residues, including Cu^{2+}-coordinating residues and water molecules. The computational details are described in *Materials and Methods* (see also *SI Appendix*, Fig. S6*A*). Relative energies of fully protonated (Full), singly deprotonated ($-H^+$), doubly deprotonated ($-2H^+$), and triply deprotonated ($-3H^+$) protonation states of the active site were extensively calculated (*SI Appendix*, Fig. S6*B*). We found that the experimentally determined crystal structure was best reproduced by the $-H^+$ state with an enolate form of TPQ in the optimized structure $\mathbf{0}^-$ (rmsd = 0.107 Å; *SI Appendix*, Table S2) and that the keto form of TPQ is accessible in the Full state (**1**) with only a slightly higher energy (3.1 kcal mol^{-1}) than the most stable enolate form of TPQ (**0**; *SI Appendix*, Table S2). The free energy change from **0** to **1** was calculated to be 0.69 kcal mol^{-1} at 298.15 K (*SI Appendix*, Table S3), well matching the value of 0.21 kcal mol^{-1} estimated from the occupancy ratio of the enolate (59%) and keto (41%) forms, although the equilibrium state in crystal could be biased by the crystal packing effects and the low temperature under the cryogenic condition (17). In agreement, the smaller rmsd value for **1** (0.167 Å), relative to that for **0** (0.251 Å), supports the formation of the keto form of TPQ (*SI Appendix*, Fig. S6*C*). Because the Full state requires one additional protonation with the active site, neutron structure and QM/MM analyses suggest that the protonation state in the active site is not unique and is, instead, mixed/extended by HB networks. We also found that the quinone ring of TPQ is bent by the HB interaction between the TPQ O5 and the carboxyl O atoms of Asp298 (O···O, ~2.9 Å; O···H, 1.9 Å; *SI Appendix*, Fig. S3*B*). The H atom between TPQ and Asp298 can also be stabilized by protonating TPQ O5 or Asp298 carboxyl O atoms (*SI Appendix*, Table S2). Therefore, this proton (deuteron) can be stabilized by the three O atoms. However, our QM/MM calculations failed to accurately reproduce the position of the triply shared proton (deuteron) that was observed in the neutron structure with bond lengths of 1.6–2.0 Å. Shared protons in LBHBs and in other short HBs were previously reported (11,

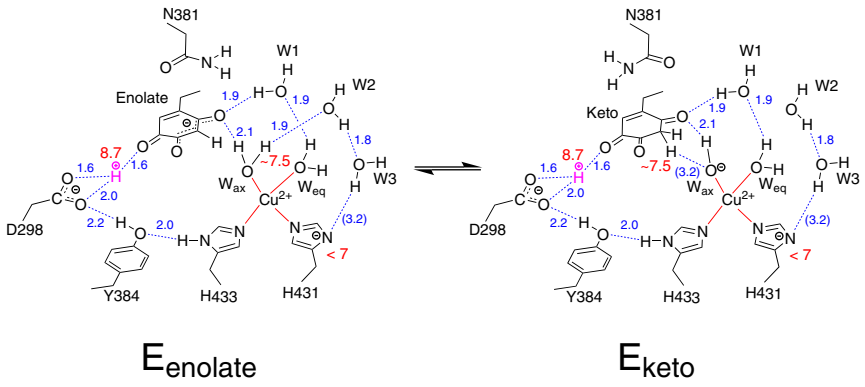

$E_{enolate}$ E_{keto}

Fig. 5. Schematic of the active-site proton network. The HB network and estimated pK_a values (red) of active-site residues are schematically depicted for the enolate form of TPQ ($E_{enolate}$) in equilibrium with the keto form of TPQ (E_{keto}). H bonds are shown as dotted lines with acceptor-H atom distances (Å) in blue; coordination bonds to the Cu^{2+} ion, red solid lines. Distances in weak H-bond-like interactions are indicated in parentheses (Å). The triply shared proton and estimated pK_a values are indicated in magenta and red, respectively (see the text in the section *Relevance of the Active-Site Structure to the Initial Step of Amine Oxidation* for details of the estimated pK_a values).

18–20). Specifically, the proton identified in photoactive yellow protein (18) was proven theoretically by taking the nuclear quantum effect of the proton into account (21), although no verification was initially achieved by QM/MM calculations (22). Thus, further ab initio simulations with precisely included nuclear quantum effects are required to describe various types of proton delocalization due to strong HBs (23).

Relevance of the Active-Site Structure to the Initial Step of Amine Oxidation. We previously demonstrated that crystalline AGAO is catalytically active and yields a semiquinone radical form of reduced TPQ following anaerobic addition of an amine substrate to crystals (8, 17). Therefore, the neutron structure determined here likely represents the initial ground state of the enzyme immediately prior to the catalytic reaction. If the steady-state kinetic parameters for the free enzyme (k_{cat}/K_m) are identical or, at least, similar in crystals and solution, pK_a values that are estimated from the bell-shaped pH dependency of k_{cat}/K_m may be assignable to active-site dissociable groups in the crystal structure. Our previous studies have shown that the ionizing groups on acid and alkaline limbs have pK_a values of 7.5 and 8.7 and must be deprotonated and protonated, respectively, before catalysis (7). These were assigned to the side-chain carboxyl group of Asp298 and the amino group of the substrate, respectively (7). We reassign these pK_a values based on the active-site structure determined here (Fig. 5). The group with pK_a of 7.5 would be assigned to the protonation of $E_{enolate}/E_{keto}$; either the protonation at TPQ C3 in $E_{enolate}$ or the protonation of W_{ax} in E_{keto}, each resulting in the same structure. Because $E_{enolate}/E_{keto}$ must accept a proton from the substrate with a protonated amino group, the protonation of $E_{enolate}/E_{keto}$ turns the enzyme into an inactive form. In accordance with this, significantly decreased SLD of one of the H atoms of W_{ax} (Fig. 4*C*) also suggests that, in $E_{enolate}$, W_{ax} with a markedly low intrinsic pK_a value of ∼7.5 (16) serves as the proton source for TPQ C3, which would have a similar intrinsic pK_a value of ∼7.5, to generate E_{keto} in equilibrium with $E_{enolate}$ (41% vs. 59%) (Fig. 5). On the other hand, an ionizing group with pK_a of 8.7 would be assigned to the triply shared proton near the midpoint of TPQ O5, Asp298 Oδ1, and Oδ2 (Fig. 3). Upon binding of the substrate and formation of the Michaelis complex, the shared proton may be released from the trifurcated state so that the deprotonated Asp298 carboxylate can accept a proton from the substrate amine ($R\text{-}NH_3^+$) (7). The released proton in the Michaelis complex may be relayed to the deprotonated His431 Nδ1 (pK_a < 7). Alternatively, the shared proton may reassociate with Asp298 carboxylate as observed in the QM/MM calculation, and the proton from the substrate may be first accepted by TPQ C3 in $E_{enolate}$ (Fig. 5) then transferred to the deprotonated His431 Nδ1. Collectively, in the extensive HB network involving TPQ and Cu^{2+} (Fig. 5), there are multiple sites that potentially accept protons in the pH region 7–9. Protons may be relayed within the active site, possibly via a Grotthuss proton hopping mechanism (24). Finally, the nonplanar quinone ring of TPQ likely reflects the strong HB between TPQ O5 and Asp298 carboxylate that is mediated by the triply shared proton. However, further theoretical studies will be required to clarify the energetic advantage for catalysis of the strained cofactor in the unliganded state as reported for the internal Schiff base of pyridoxal 5′-phosphate in aspartate aminotransferase (25).

To summarize, after nearly 30 years since the chemical structure of the sophisticated protein-derived cofactor TPQ was determined (26), we have established its true structure and the associated proton network in the CAO active site using neutron crystallography. As the ionized form of the lightest atom, protons often display quantum behaviors, such as delocalization (proton sharing) and tunneling, which have been observed in a number of enzyme systems (27, 28). Neutron crystallography provides an essential structural basis to elucidate these quantum effects of protons that are of great interest in studies of enzyme catalysis.

Materials and Methods

Preparation of Huge AGAO Crystals and Postcrystallization Treatment. Recombinant AGAO was purified as the Cu^{2+}-free precursor form and converted to the Cu^{2+}/TPQ-containing active form as reported previously (7). The enzyme was crystallized by a modified hanging method, which was optimized for preparing high-quality and extra large crystals. The enzyme (concentration, 30 mg/mL) was dialyzed in a 350-μL microdialysis button (diameter, 1 cm) at 16 °C against 20 mL of 1.05-M potassium sodium (Na) tartrate in 25-mM 4-(2-hydroxyethyl)-1-piperazineethanesulfonic acid buffer, pH 7.4, with the dialysis membrane facing down to the bottom of the sealed vessel for a week followed by turning the button upside down for additional 3 to 4 wk until crystals grow up to a size of about 5.0 × 2.0 × 1.0 mm (*SI Appendix*, Fig. S1*A*). For the neutron diffraction measurement, the dialysis buttons were transferred into a 50-mL vessel containing 20 mL of 3.0-M deuterated malonate solution, pD 7.4, for cryoprotection and deuteration (29). The soaking solution (D, >98%) was prepared by dissolving malonate-D4 (powder; D, 98%) in D_2O (D, 99.9%) and adjusting the pD to 7.4 with a NaOD solution (D, 99.5%). pD values were determined by adding a value of 0.4 to the direct reading of a pH meter calibrated in H_2O. All deuterated reagents were purchased from Cambridge Isotope Laboratories, Inc. The soaking solution was exchanged twice in 4 wk to achieve complete H/D exchange. The crystals were then mounted on a thin nylon loop (ø, 3.0 mm) and frozen by flash cooling to 100 K in a cold N_2 gas stream (*SI Appendix*, Fig. S1*B*).

Neutron Diffraction Experiment. Time-of-flight (TOF) neutron diffraction data collection was carried out in BL03, Ibaraki biological crystal diffractometer iBIX, at the Materials and Life Science Experimental Facility (MLF) of the Japan Proton Accelerator Research Complex (J-PARC, Tokai, Japan) (30, 31). The diffraction data sets were collected at 100 K with 30 wavelength-shift-fiber type detectors having a sensor area of 133 × 133 mm and being placed at 2θ center from 20.3° to 161°. A total of 33 datasets were collected using a neutron pulse beam at wavelengths of 3.0–5.6 Å with a detector distance of 491.1 mm. Exposure time for each data set was 5.1 h at 500 kW (17 sets) and 11.1 h at 200 kW (16 sets). The TOF neutron diffraction data were indexed, integrated, merged, and scaled up to 1.72-Å resolution using STARGazer (32, 33). After collection of neutron diffraction data, the same crystal was used for subsequent X-ray diffraction experiments.

X-ray Diffraction Experiment. X-ray diffraction data were collected using a Quantum315r CCD detector (ADSC, California, USA) at 100 K at BL5A in the Photon Factory (Tsukuba, Japan). The wavelength of the synchrotron radiation and oscillation range were 1.0 Å and 1.0°, respectively. To cover the entire range of intensities, the subatomic resolution data were collected as three sets of diffraction measurements with differing crystal-to-detector distances (90.93, 213.47, and 284.66 mm). To minimize the radiation damage, the position of the crystal during irradiation was changed in each shot. A total of 540 images was collected. Data were integrated, merged, and scaled up to 1.14-Å resolution using HKL2000 software (34). Statistics of the neutron and X-ray diffraction data are summarized in *SI Appendix*, Table S1.

Structure Refinement. The starting model was obtained by molecular replacement with Phaser (35) for X-ray data. The coordinates of the AGAO monomer (3WA2) (36) were used as a search model after removing all water and ligand molecules. Refinements, calculation of ED maps, and assignment of solvent molecules were performed initially using Phenix version 1.11 (37) only with X-ray diffraction data. Manual rebuilding was performed using Coot, and water molecules were added step by step to the model during the refinement. Then, joint refinement was performed with both the neutron and the X-ray diffraction data using Phenix version 1.11. The protonation (deuteronation) states of amino acid residues and the orientation of water molecules were manually adjusted by carefully examining SLD on Coot (38) before including H/D atoms in the refinement calculation. The position and temperature factors of all H/D atoms were refined individually using Phenix version 1.11, together with the occupancy refinement. The model of the keto form of TPQ was built using the PRODRG server (http://davapc1.bioch.dundee.ac.uk/prodrg/) (39) and used for refinement, assuming that the keto form of TPQ coexists with the original enolate form. Water molecules were finally verified by Phenix with default parameters. The Ramachandran plot was calculated using MolProbity (40) for structure validation. The refinement statistics are represented in *SI Appendix*, Table S1. PyMOL version

1.8 (Schrödinger, LLC) was used for figure drawings. Atomic coordinates and structure factors of the AGAO neutron structure are available at the Protein Data Bank (http://www.rcsb.org/) (accession no. 6L9C).

Computational Details. The initial atomic coordinates were taken from the neutron structure of AGAO including H/D coordinates determined in the present paper. After checking the protonation states for amino acid residues and selecting a model in higher occupancies, one subunit model with TPQ was constructed. The entire system was charge neutralized by placing 21 Na^+ ions as counterions, and the system was solvated by a water droplet with a 60-Å radius. The system was relaxed at a molecular mechanics level. The relaxation is composed of 1-ps molecular dynamics (MD) simulation at 298.15 K and the following 1-ps annealing MD from 298.15 to 0 K. In both MDs, added solvent water molecules and all H atoms except for the two C3 H atoms of the keto form TPQ and a dissociable H atom of the Asp298 carboxyl group in the initial crystal structure were allowed to move.

After the above-described MD, hybrid QM/MM calculations were performed. For the QM region, side chains of Tyr284, Asp298, Tyr384, Asn381, TPQ, His431, His433, His592, Cu^{2+} ion, and four water molecules were included (*SI Appendix*, Fig. S6*A*). The theoretical level used for the QM/MM calculation was UB3LYP-D3/DZVP|Amberff99, which means that the unrestricted hybrid DFT of the B3LYP exchange-correlation function with Grimme's D3 dispersion correction (41) was used for the QM region, and the Amberff99 force field was used for the MM region. The DZVP basis set represents valence double-ζ plus polarized level basis sets, LANL-2DZ for Cu and 6–31G* for other atoms (42–44). UB3LYP-D3/DZVP level calculations properly reproduce geometric structures and fine magnetic interactions for transition metal complexes and enzymes as shown in our previous reports (45, 46). The same MM force field parameters were used for the initial MD relaxations.

Geometry optimizations were performed for all atoms within a 15-Å radius of a fixed QM center. H link atoms were employed for the QM/MM boundary. An electronic embedding scheme was adopted, and nonbonded interactions were not cut off for the QM/MM interactions (no cutoff). All of the theoretical calculations, MD, and QM/MM were performed by using the NWChem 6.3 program package (47).

ACKNOWLEDGMENTS. We acknowledge the facility staff. This work was performed using neutron beamline station, Ibaraki biological crystal diffractometer iBIX (BL03) at MLF of J-PARC with approval from J-PARC Center (Proposals 2014A0249, 2015A0070). Synchrotron X-ray beamline station BL5A at the Photon Factory was used with approval from High Energy Accelerator Research Organization (Proposal 2016G516). Synchrotron X-ray beamline stations BL44XU and BL38B1 at the SPring-8 facility were used under the Cooperative Research Program of the Institute for Protein Research, Osaka University (Proposals 2017B6709, 2018A6807, and 2018B6807) and with approval from the Japan Synchrotron Radiation Institute (Proposals 2014B1148, 2015A1065, 2016A2522, and 2017A2544), respectively. Numerical calculations were carried out under the support of (1) Multidisciplinary Cooperative Research Program in CCS, University of Tsukuba, and (2) HPCI system research project (Project hp19110) using the computational resource of CX400 provided by the Information Technology Center in Nagoya University. This work was supported by JSPS KAKENHI Grants JP23770127 and JP26440037 to T.M., JP15K05573 to H.H., and JP16KT0055 and 19K05694 to T.O. from Japan Society for the Promotion of Science and by funding from the Network Joint Research Center for Materials and Devices.

1. M. Eigen, Proton transfer, acid-base catalysis, and enzymatic hydrolysis. Part I: Elementary processes. *Angew. Chem. Int. Ed. Engl.* **3**, 1–19 (1964).
2. F. Shu, V. Ramakrishnan, B. P. Schoenborn, Enhanced visibility of hydrogen atoms by neutron crystallography on fully deuterated myoglobin. *Proc. Natl. Acad. Sci. U.S.A.* **97**, 3872–3877 (2000).
3. A. Nakamura *et al.*, "Newton's cradle" proton relay with amide-imidic acid tautomerization in inverting cellulase visualized by neutron crystallography. *Sci. Adv.* **1**, e1500263 (2015).
4. W. B. O'Dell, A. M. Bodenheimer, F. Meilleur, Neutron protein crystallography: A complementary tool for locating hydrogens in proteins. *Arch. Biochem. Biophys.* **602**, 48–60 (2016).
5. G. Floris, B. Mondovi, Eds., *Copper Amine Oxidases: Structures, Catalytic Mechanisms and Role in Pathophysiology*, (C.R.C. Press, Inc., Boca Raton, FL, 2009).
6. T. Murakawa *et al.*, Quantum mechanical hydrogen tunneling in bacterial copper amine oxidase reaction. *Biochem. Biophys. Res. Commun.* **342**, 414–423 (2006).
7. Y. C. Chiu *et al.*, Kinetic and structural studies on the catalytic role of the aspartic acid residue conserved in copper amine oxidase. *Biochemistry* **45**, 4105–4120 (2006).
8. T. Murakawa *et al.*, Probing the catalytic mechanism of copper amine oxidase from *Arthrobacter globiformis* with halide ions. *J. Biol. Chem.* **290**, 23094–23109 (2015).
9. M. Adachi *et al.*, Structure of HIV-1 protease in complex with potent inhibitor KNI-272 determined by high-resolution X-ray and neutron crystallography. *Proc. Natl. Acad. Sci. U.S.A.* **106**, 4641–4646 (2009).
10. W. W. Cleland, Low-barrier hydrogen bonds and enzymatic catalysis. *Arch. Biochem. Biophys.* **382**, 1–5 (2000).
11. M. T. Banco *et al.*, Neutron structures of the *Helicobacter pylori* 5′-methylthioadenosine nucleosidase highlight proton sharing and protonation states. *Proc. Natl. Acad. Sci. U.S.A.* **113**, 13756–13761 (2016).
12. M. C. J. Wilce *et al.*, Crystal structures of the copper-containing amine oxidase from *Arthrobacter globiformis* in the holo and apo forms: Implications for the biogenesis of topaquinone. *Biochemistry* **36**, 16116–16133 (1997).
13. T. E. Creighton, *Proteins: Structures and Molecular Properties*, (W. H. Freeman and Company, New York, 1993).
14. K. Hasegawa, T. Ono, T. Noguchi, Vibrational spectra and ab initio DFT calculations of 4-methylimidazole and its different protonation forms: Infrared and Raman markers of the protonation state of a histidine side chain. *J. Phys. Chem. B* **104**, 4253–4265 (2000).
15. R. Hienerwadel, C. Berthomieu, Bicarbonate binding to the non-heme iron of photosystem II investigated by Fourier transform infrared difference spectroscopy and ^{13}C-labeled bicarbonate. *Biochemistry* **34**, 16288–16297 (1995).
16. J. Kyte, *Mechanism in Protein Chemistry*, (Garland Publishing, Inc., New York, 1995).
17. T. Murakawa *et al.*, *In crystallo* thermodynamic analysis of conformational change of the topaquinone cofactor in bacterial copper amine oxidase. *Proc. Natl. Acad. Sci. U.S.A.* **116**, 135–140 (2019).
18. S. Yamaguchi *et al.*, Low-barrier hydrogen bond in photoactive yellow protein. *Proc. Natl. Acad. Sci. U.S.A.* **106**, 440–444 (2009).
19. O. Gerlits *et al.*, Long-range electrostatics-induced two-proton transfer captured by neutron crystallography in an enzyme catalytic site. *Angew. Chem. Int. Ed. Engl.* **55**, 4924–4927 (2016).
20. P. Kumar, E. H. Serpersu, M. J. Cuneo, A low-barrier hydrogen bond mediates antibiotic resistance in a noncanonical catalytic triad. *Sci. Adv.* **4**, eaas8667 (2018).
21. M. Nadal-Ferret, R. Gelabert, M. Moreno, J. M. Lluch, Are there really low-barrier hydrogen bonds in proteins? The case of photoactive yellow protein. *J. Am. Chem. Soc.* **136**, 3542–3552 (2014).
22. K. Saito, H. Ishikita, Energetics of short hydrogen bonds in photoactive yellow protein. *Proc. Natl. Acad. Sci. U.S.A.* **109**, 167–172 (2012).
23. L. Wang, S. D. Fried, S. G. Boxer, T. E. Markland, Quantum delocalization of protons in the hydrogen-bond network of an enzyme active site. *Proc. Natl. Acad. Sci. U.S.A.* **111**, 18454–18459 (2014).
24. S. Dajnowicz *et al.*, Direct evidence that an extended hydrogen-bonding network influences activation of pyridoxal 5′-phosphate in aspartate aminotransferase. *J. Biol. Chem.* **292**, 5970–5980 (2017).
25. H. Hayashi, H. Mizuguchi, H. Kagamiyama, The imine-pyridine torsion of the pyridoxal 5′-phosphate Schiff base of aspartate aminotransferase lowers its pK_a in the unliganded enzyme and is crucial for the successive increase in the pK_a during catalysis. *Biochemistry* **37**, 15076–15085 (1998).
26. S. M. Janes *et al.*, A new redox cofactor in eukaryotic enzymes: 6-hydroxydopa at the active site of bovine serum amine oxidase. *Science* **248**, 981–987 (1990).
27. M. J. Sutcliffe, N. S. Scrutton, A new conceptual framework for enzyme catalysis. Hydrogen tunnelling coupled to enzyme dynamics in flavoprotein and quinoprotein enzymes. *Eur. J. Biochem.* **269**, 3096–3102 (2002).
28. J. P. Klinman, A. Kohen, Hydrogen tunneling links protein dynamics to enzyme catalysis. *Annu. Rev. Biochem.* **82**, 471–496 (2013).
29. T. Holyoak *et al.*, Malonate: A versatile cryoprotectant and stabilizing solution for salt-grown macromolecular crystals. *Acta Crystallogr. D Biol. Crystallogr.* **59**, 2356–2358 (2003).
30. I. Tanaka *et al.*, Neutron structure analysis using the IBARAKI biological crystal diffractometer (iBIX) at J-PARC. *Acta Crystallogr. D Biol. Crystallogr.* **66**, 1194–1197 (2010).
31. K. Kusaka *et al.*, Evaluation of performance for IBARAKI biological crystal diffractometer iBIX with new detectors. *J. Synchrotron Radiat.* **20**, 994–998 (2013).
32. T. Ohhara *et al.*, Development of data processing software for a new TOF single crystal neutron diffractometer at J-PARC. *Nucl. Instrum. Methods Phys. Res. Sect. A Accel. Spectrometers. Detect. Assoc. Equip.* **600**, 195–197 (2009).
33. N. Yano *et al.*, Status of the neutron time-of-flight single-crystal diffraction data-processing software STARGazer. *Acta Crystallogr. D Struct. Biol.* **74**, 1041–1052 (2018).
34. Z. Otwinowski, W. Minor, Processing of X-ray diffraction data collected in oscillation mode. *Methods Enzymol.* **276**, 307–326 (1997).
35. A. J. McCoy *et al.*, Phaser crystallographic software. *J. Appl. Cryst.* **40**, 658–674 (2007).
36. T. Murakawa *et al.*, High-resolution crystal structure of copper amine oxidase from *Arthrobacter globiformis*: Assignment of bound diatomic molecules as O_2. *Acta Crystallogr. D Biol. Crystallogr.* **69**, 2483–2494 (2013).
37. P. D. Adams *et al.*, *PHENIX*: A comprehensive python-based system for macromolecular structure solution. *Acta Crystallogr. D Biol. Crystallogr.* **66**, 213–221 (2010).
38. P. Emsley, B. Lohkamp, W. G. Scott, K. Cowtan, Features and development of Coot. *Acta Crystallogr. D Biol. Crystallogr.* **66**, 486–501 (2010).

39. A. W. Schüttelkopf, D. M. F. van Aalten, *PRODRG*: A tool for high-throughput crystallography of protein-ligand complexes. *Acta Crystallogr. D Biol. Crystallogr.* **60**, 1355–1363 (2004).
40. V. B. Chen *et al*., *MolProbity*: All-atom structure validation for macromolecular crystallography. *Acta Crystallogr. D Biol. Crystallogr.* **66**, 12–21 (2010).
41. S. Grimme, J. Antony, S. Ehrlich, H. Krieg, A consistent and accurate *ab initio* parametrization of density functional dispersion correction (DFT-D) for the 94 elements H-Pu. *J. Chem. Phys.* **132**, 154104 (2010).
42. P. J. Hay, W. R. Wadt, *Ab initio* effective core potentials for molecular calculations. Potentials for the transition metal atoms Sc to Hg. *J. Chem. Phys.* **82**, 270–283 (1985).
43. P. J. Hay, W. R. Wadt, *Ab initio* effective core potentials for molecular calculations. Potentials for main group elements Na to Bi. *J. Chem. Phys.* **82**, 284–298 (1985).
44. P. J. Hay, W. R. Wadt, *Ab initio* effective core potentials for molecular calculations. Potentials for K to Au including the outermost core orbitals. *J. Chem. Phys.* **82**, 299–310 (1985).
45. M. Shoji, H. Isobe, J.-R. Shen, K. Yamaguchi, Geometric and electronic structures of the synthetic Mn_4CaO_4 model compound mimicking the photosynthetic oxygen-evolving complex. *Phys. Chem. Chem. Phys.* **18**, 11330–11340 (2016).
46. M. Shoji *et al*., A QM/MM study of the L-threonine formation reaction of threonine synthase: Implications into the mechanism of the reaction specificity. *J. Am. Chem. Soc.* **136**, 4525–4533 (2014).
47. M. Valiev *et al*., NWChem: A comprehensive and scalable open-source solution for large scale molecular simulations. *Comput. Phys. Commun.* **181**, 1477–1489 (2010).